



# Modeling of large deformations effect on non-linear response in composite bending beams through finite elements and a novel analytical method

Juan Macías\*, Santiago Marín, Juan Meza

Universidad Nacional de Colombia, DADCOMP - Design of advanced composites, Carrera 65 No. 59A - 110, Medellín, 050034, Colombia

## ARTICLE INFO

**Keywords:**  
 Composite materials  
 Bending test  
 Large deformations  
 Finite elements  
 Analytical modeling  
 ASTM D6272

## ABSTRACT

This paper presents a novel analytical model for predicting the behavior of composite materials under three- and four-point bending tests and large deformations. The model adapts a previous isotropic formulation to account for anisotropic behavior and contact interaction. The model was validated with experimental data reported in the literature using hybrid composite materials and quasi-isotropic laminates, obtaining accurate predictions of global reaction loads, deformation, and strain measurements. Moreover, 3D shell and 2D plane strain finite element models were developed to verify the analytical model and to study the effects of large deformations on the non-linear response of composite beams. It was found that before the first drop in the load-deflection curve, most of the non-linear behavior of the investigated materials is mainly due to geometrical effects and not to damage. Finally, the implications of geometric non-linearities in the ASTM D6272 standard stress calculations were discussed, and some limitations were highlighted.

## 1. Introduction

Plastic-reinforced composite materials offer many advantages over traditional isotropic materials in structural applications because of their higher strength and stiffness-to-weight ratio, corrosion resistance, and improved fatigue behavior [1]. However, their nature is mainly brittle; sudden failure is usually expected, which implies more extensive testing campaigns and higher safety factors within the design process. These imply higher production costs and reduction in weight-saving capabilities [2]. Therefore, creating models that accurately predict the behavior of such materials is essential to increase their applicability by cutting down on the physical testing requirements.

To predict the behavior of beams in three- and four-point bending tests, it is common to use analytical solutions based on the classical beam theory, which deals with both infinitesimal strains and infinitesimal deformation assumptions [3]. This kind of solution may capture the essential characteristics when modeling thick and rigid beams under relatively small deformations and very conservative span-to-thickness ratios (STR), as recommended by the standards, like 32:1 and 16:1 [4, 5]. However, when it comes to composite laminates, the thickness of the laminates is usually lower than recommended (< 4 mm), and it is necessary to use larger STR of up to 40:1 and 60:1 to prevent shear failure, which is one of the failure modes that needs to be avoided when the characterization of the longitudinal and transversal properties of the composite layup is performed using bending tests [4,5]. In these conditions, large deformations can be evidenced in the specimens under

relatively small loads while keeping sub-critical stresses and strains. Although the standard suggests some methods to calculate mechanical properties in these circumstances, due to the large deflections of the specimens, the results obtained with these methods may be inaccurate as a consequence of geometric non-linear effects that can heavily pollute the stress and strain approximations computed according to the equations given by standards like ASTM D6272-17e1 or ASTM D7264 / D7264M-21 [4,5].

It is currently possible to use Finite Elements (FE) models to understand and predict the non-linear behavior of composite laminates, including hybrids, under three- and four-point bending tests. Some of these FE models use a 3D shell element approach [6] or a 2D plane strain approach [7–12]. To simplify the simulations, most of these models do not consider the geometric non-linearities and avoid the contact interaction between the specimen, the upper cylinders and the lateral supports. Although FE models can give reliable results when used correctly, they require high computational resources and simulation time, especially when considering contact interaction and non-linearities. For this reason, different numerical and analytical modeling approaches are continuously being developed to avoid the computational cost of FE predictions. Some models that account for non-linearities and large deformations can also consider failure (including micro-buckling or micro-structural defects) using multi-scale analysis [13–16], which are typically validated or verified with experimental tests or FE models.

\* Corresponding author.

E-mail address: [jmmaciasl@unal.edu.co](mailto:jmmaciasl@unal.edu.co) (J. Macías).

Some authors have proposed analytical models for predicting the non-linear behavior during bending tests [17,18]. However, these models are limited because they can only be used for symmetric laminates of composite materials under three-point bending tests. Another proposed approach is to use the mathematical model for the three-point composite bending test developed in [19]. However, the model's reliability is unknown because it has not been experimentally validated.

This work introduces a novel analytical model for predicting the elastic behavior of composite beams when subjected to three- and four-point bending loading. The model considers the non-linear behavior produced by large deformations. It can be easily implemented and it provides results with a reduced computational cost if compared to numerical tools such as the Finite Element Method. The model is a continuation of the non-linear beam theory developed by Paolinis and Ogorkiewicz in [20]. It was modified to account for orthotropic material behavior using the main pillars of the Classical Laminate Theory (CLT), this addition is necessary in order to model specimens made of composite layups with different stacking sequences. Unlike previous publications, the new formulation can cope with unbalanced staking sequences and hybrid layups. Moreover, it was modified to consider changes in the contact points between the specimen and the machine supports during the bending test. The model was also adjusted to be used in three- and four-point bending test configurations. To the author's knowledge, these last features have not been considered before in any of the analytical models found in the literature review.

This paper is organized as follows. Section 2 reviews the CLT, and Paolinis and Ogorkiewicz theories. Then, starting from Paolinis and Ogorkiewicz core formulation, the additions and modifications that compose the new analytical model are explained in detail. Section 3 is dedicated to the validation and verification of the robustness and efficiency of the proposed analytical model, as well as the finite element approaches (2D plain strain and 3D shell models) using the experimental results on three- and four-point bending test of quasi-isotropic and hybrid layups. Finally, in Section 4, the numerical and analytical models are used to evaluate the accuracy of the ASTM standard to predict the stress-strain behavior and the maximum stress under large STRs.

## 2. Analytical model development

### 2.1. Classical laminate theory (CLT)

The Classical Laminate Theory (CLT) defines the relationships between the structural properties of the macro-scale laminate in terms of the meso-scale material, orientation, and stacking sequence of the plies that constitute such laminate. This theory shows these associations in the form of a relationship between the in-plane forces and moments per unit width applied to a rectangular section of the laminate, and the strains and curvatures induced [21]. It has been found that this is one of the most widely used methodologies for modeling stiffness and first/last ply failure analysis of standard and even hybrid composite laminates, and in general, for modeling the behavior and failure of thin layered materials loaded as panels or membranes [6,21,22]. Furthermore, this theory is the backbone of the analytical approaches to study the hybrid effect in composite laminates [6,23] and is implemented within the FE formulation of the shell elements, the main computational tool to study composite materials at the meso-scale [22].

There are some essential conventions to follow regarding coordinate systems. The laminate is modeled as a plate or shell under plane stress with global coordinates defined as  $(x, y, z)$ . The  $x$  and  $y$  coordinates correspond to the length and width of the plate, which are much larger than the thickness – defined in the  $z$  coordinate –. The local ply coordinates are defined as  $(1, 2, 3)$ , where 1 and 2 correspond to the fiber and transversal directions of the ply, and 3 corresponds to the thickness. The orientation of each lamina is defined as the angle between the 1 local axis and the  $x$  axis, where  $z$  and 3 axes are always parallel.

Stresses are defined in the laminate coordinate system according to the traditional convention explained in [1] where the first index refers to the load direction and the second one to the plane where the load is acting. Therefore, equal indexes represent normal stresses, and different indexes refer to shear stresses. The strains in the laminate coordinates follow the same convention.

The CLT relies on some base assumptions, the first being that the thickness of the laminate is much smaller than the other dimensions. Also, it is important to assume that the out-of-plane stresses ( $\sigma_z$ ) and strains ( $\epsilon_z$ ) are small enough to be considered equal to zero. Besides, the in-plane shear stress ( $\gamma_{xy}$ ) is constant through the thickness, and local deformation is small enough to consider infinitesimal strains. In the CLT, the displacement of a composite plate is described at every point as follows:

$$\mathbf{u}(x, y, z) = \mathbf{u}_0(x, y) + z\varphi_x(x, y) \quad (1)$$

$$\mathbf{v}(x, y, z) = \mathbf{v}_0(x, y) - z\varphi_y(x, y) \quad (2)$$

Where  $\mathbf{u}$  and  $\mathbf{v}$  are the displacements – i.e., change of position – in the  $x$ -direction and  $y$ -direction, respectively, at every point  $(x, y, z)$ ;  $\mathbf{u}_0$  and  $\mathbf{v}_0$  are the displacements of every point  $(x, y)$  located at the middle surface, and  $\varphi_x$  and  $\varphi_y$  are the rotation angles of the plate middle surface with respect to a vertical line. From the definition of the infinitesimal strain tensor [24], the strain–displacement relationship can be defined as follows:

$$\epsilon_x(x, y, z) = \frac{\partial \mathbf{u}_0}{\partial x} - z \frac{\partial \varphi_x}{\partial x} \quad (3)$$

$$\epsilon_y(x, y, z) = \frac{\partial \mathbf{v}_0}{\partial y} - z \frac{\partial \varphi_y}{\partial y} \quad (4)$$

$$\gamma_{xy}(x, y, z) = \frac{\partial \mathbf{u}_0}{\partial y} + \frac{\partial \mathbf{v}_0}{\partial x} - z \left( \frac{\partial \varphi_x}{\partial y} + \frac{\partial \varphi_y}{\partial x} \right) \quad (5)$$

Which can be simplified by using the matrix form:

$$\begin{Bmatrix} \epsilon_x \\ \epsilon_y \\ \gamma_{xy} \end{Bmatrix} = \begin{Bmatrix} \epsilon_x^0 \\ \epsilon_y^0 \\ \gamma_{xy}^0 \end{Bmatrix} - z \begin{Bmatrix} \kappa_x \\ \kappa_y \\ \kappa_{xy} \end{Bmatrix} \quad (6)$$

Where  $\epsilon_x^0$ ,  $\epsilon_y^0$ , and  $\gamma_{xy}^0$  are the middle-surface strains;  $\kappa_x$  and  $\kappa_y$  are the bending curvatures and  $\kappa_{xy}$  is the torsional curvature. From here on, it follows to define the stress distribution as:

$$\begin{Bmatrix} \sigma_x \\ \sigma_y \\ \sigma_{xy} \end{Bmatrix} = [\bar{Q}] \begin{Bmatrix} \epsilon_x \\ \epsilon_y \\ \gamma_{xy} \end{Bmatrix} \quad (7)$$

Where  $[\bar{Q}]$  is the plane stress stiffness matrix for a lamina as rotated in the global (laminate) coordinate system, which can be obtained from the in-plane material properties of the lamina and its orientation.

The strain distribution is assumed uniform throughout the whole laminate. However, as every lamina may have a different stiffness or orientation, the resultant stress distribution is only piece-wise continuous. The external forces and moments per unit length acting at the boundary of the laminate plate can be found by integrating the stress through the laminate thickness to yield the following relationship.

$$\begin{Bmatrix} N_x \\ N_y \\ N_{xy} \\ M_x \\ M_y \\ M_{xy} \end{Bmatrix} = [\mathbf{A}] \begin{Bmatrix} \mathbf{B} \\ \mathbf{D} \end{Bmatrix} \begin{Bmatrix} \epsilon_x^0 \\ \epsilon_y^0 \\ \gamma_{xy}^0 \\ \kappa_x \\ \kappa_y \\ \kappa_{xy} \end{Bmatrix} \quad (8)$$

Where  $N_i$  and  $M_i$  are the external forces and moments per unit length along the side of the plate,  $[\mathbf{A}]$  is the in-plane stiffness matrix, which relates the in-plane strains to in-plane forces;  $[\mathbf{B}]$  is the bending-extension coupling matrix, which relates in-plane forces with out-of-plane curvatures, and out-of-plane external moments with in-plane strains; and  $[\mathbf{D}]$

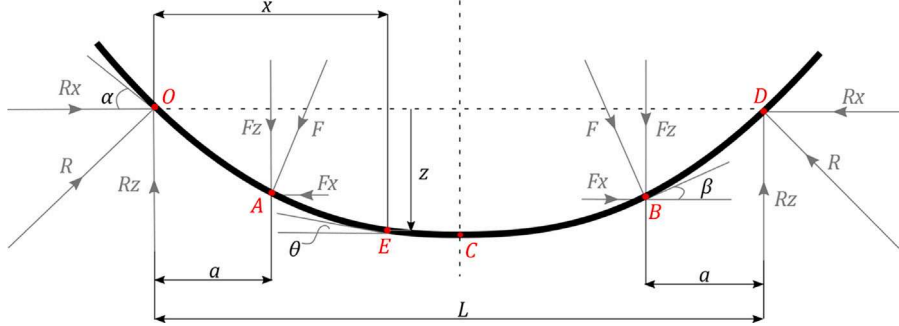


Fig. 1. Free body diagram of a four-point bending beam under large deformations [20].

is the bending stiffness matrix, which relates the applied moments to curvatures on the laminate.

The terms of the **ABD** matrices can be obtained as such:

$$A_{ij} = \sum_{k=1}^N \bar{Q}_{ij}^k (z_k - z_{k-1}) \quad (9)$$

$$B_{ij} = -\frac{1}{2} \sum_{k=1}^N \bar{Q}_{ij}^k (z_k^2 - z_{k-1}^2) \quad (10)$$

$$D_{ij} = \frac{1}{3} \sum_{k=1}^N \bar{Q}_{ij}^k (z_k^3 - z_{k-1}^3) \quad (11)$$

For  $i, j = 1, 2, 6$ ; where  $N$  refers to the number of plies in the laminate,  $\bar{Q}_{ij}$  is the transformed reduced stiffness matrix of each ply,  $k$  (which is used as a superscript, not to be confused with an exponent), and  $z$  refers to the position of the ply in the thickness direction of the laminate. The full derivation of the CLT is detailed in [1].

The **ABD** matrix can be obtained from the constituent properties, stacking sequence, and orientations. It represents the stiffness of a unit-length shell of the laminate material. This way, either the resulting deformation due to an applied load state or the resulting reaction forces due to an imposed deformation state can be obtained. In fact, given that they are mutually exclusive, any choice of known and unknown variables can be made, and the algebraic system can still be solved.

## 2.2. Composite beams large deflections analytical model

Although the model proposed by Paolinelis and Ogorkiewicz in [20] already considers possible non-linearities in the analytical solution for the four-point bending test, the model was modified to account contact interactions that can vary their position during the test, because they are also a source of non-linear behavior and large deformations. Moreover, the new model is adapted to capture both three- and four-point bending tests and to consider the bending compliance in terms of the laminate stiffness parameters. This represents an extension from isotropic materials to laminate composites. The work done in [20] was initially derived to compute the load-displacement behavior of an isotropic thin beam under large deformations and the following assumptions were considered:

- Large deformations are present while small strains are kept.
- The material is homogeneous and its behavior is linear elastic.
- Load application points (O, A, B, and D in Fig. 1) do not move in the  $x$  direction during deformation.

The derivation found in [20] provides a relation between the applied force at the upper cylinders (Points A and B in Fig. 1), reaction loads at the lateral supports (Points O and D in Fig. 1), and the vertical displacement  $Z$  at every point along the beam's length [20]. Thus,

the lateral support reactions and beam stiffness can be related to the geometric parameters of the deformation through Eqs. (12) and (13).

$$\left( \frac{2R}{EI} \right)^{1/2} a = 2 \cos(\alpha) \sin^{1/2}(\alpha - \beta) + \sin(\alpha) P(\alpha - \beta) \quad (12)$$

$$\left( \frac{2R}{EI} \right)^{1/2} z_a = 2 \sin(\alpha) \sin^{1/2}(\alpha - \beta) + \cos(\alpha) P(\alpha - \beta) \quad (13)$$

Where  $R$  is the lateral support reaction,  $a$  is the distance between the lateral support and the upper cylinders,  $z_a$  is the vertical displacement of the upper cylinders,  $\alpha$ , and  $\beta$  are the angles formed by the beam deflection, and a horizontal line at the contact point with the lateral support and the upper cylinders, respectively. The function  $P(\alpha - \beta)$  is defined in Eq. (14). The product  $EI$  is defined as the isotropic material Young's modulus times the second moment of area of the beam's cross-section referred to as its neutral axis; this product represents the stiffness of the beam, accounting for both material and cross-section shape. Using the CLT, such representative beam stiffness can be redefined with the laminate parameters. Namely, if the beam is made of a laminate oriented as shown in Fig. 1 the product  $EI$  can be related to the ratio  $M_x / (\kappa_x)$  using Eq. (8), where the remaining laminate loads are set as zero (the vertical displacement of the upper cylinders does not create additional in-plane loads).

$$P(\alpha - \beta) = \int_{\phi=0}^{\phi=\alpha-\beta} \sin^{1/2} \phi d\phi \quad (14)$$

The curvature of the beam in the central region (area between the upper cylinders) is defined by Eq. (15).

$$\frac{1}{r} = \left[ \frac{2R}{EI} \frac{\sin(\alpha - \beta) \cos(\theta)}{\cos(\beta)} \right]^{\frac{1}{2}} \quad (15)$$

Where  $1/r = \kappa_x$  is the curvature of the beam, initially defined in the CLT in Eq. (8). Likewise,  $\theta$  is the angle with respect to the horizontal line at any point in the beam between the upper cylinders; see Fig. 2. The curvature and angle vary along the beam's length; while the curvature reaches its maximum at the middle of the beam span, the  $\theta$  angle reaches its minimum at this point. The Bernoulli–Euler hypothesis is assumed to hold, so “*the plane sections originally normal to the centroidal axis of the beam remain plane and normal to its deformed axis*” [20], giving Eq. (16).

$$M = \frac{EI}{r} \quad (16)$$

Where the applied bending moment due to the upper cylinder and lateral support loads is  $M$  equivalent to  $M_x$  in the CLT in Eq. (8). The geometric relationship between the angles  $\alpha$  and  $\beta$ , the distance between the upper cylinders and lateral supports  $a$ , and lateral support

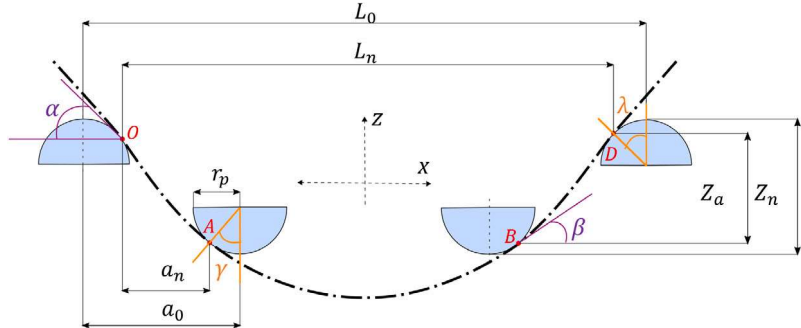


Fig. 2. Schematic of a thin beam under large displacements in a four-point bending test.

span  $L$  is given by Eq. (17).

$$\frac{L}{2a} - 1 = \frac{\left\{ \frac{\cos(\beta)}{\sin(\alpha-\beta)} \right\}^{\frac{1}{2}} \varphi(\beta)}{2 \cos(\alpha) \sin^{1/2}(\alpha-\beta) + \sin(\alpha) P(\alpha-\beta)} \quad (17)$$

Where the function  $\varphi(\beta)$  is defined by Eq. (18).

$$\varphi(\beta) = \int_{\phi=0}^{\phi=\beta} \cos^{1/2}(\phi) d\phi \quad (18)$$

The relationship between the load at the upper cylinders ( $F$ ) and reaction force at the lateral supports ( $R$ ) is given by the equilibrium condition according to Eq. (19).

$$F \cos(\beta) = R \cos(\alpha) \quad (19)$$

The main modification to these equations is to account for the variation of the contact points by considering that the upper cylinders and lateral supports have a finite radius  $r_p$ . The values of  $L$ ,  $a$ , and  $z_a$  should be considered not as constants but rather as variables depending on  $\alpha$ ,  $\beta$  and  $r_p$ . Following this idea, the notation changes according to Fig. 2. From here on, the constant values of  $L$  and  $a$  are replaced by the introduction of new variables called  $L_n$  and  $a_n$  respectively. In the new formulation, the values of  $L_n$  and  $a_n$  evolve according to Eqs. (20) and (21), respectively. It means that, as deformation progresses, the values of  $\alpha$  and  $\beta$  increase as before; but now, the contact points move around the perimeter of the upper cylinders and lateral supports. For the lateral supports, the contact point moves around the perimeter from 0 to  $\lambda$ ; see Fig. 2. Consequently the effective lateral support distance  $L_n$  is gradually reduced as the value of  $\alpha$  increases and depends also on the lateral support radius  $r_p$ . On the other hand, for the upper cylinders, the contact point moves around the perimeter from 0 to  $\gamma$ ; see Fig. 2. The distance  $a_n$  is reduced when both  $\alpha$  and  $\beta$  increase; such reduction in  $a_n$  is also related to the upper cylinders and lateral support radius  $r_p$ . In the same way, the vertical displacement of the upper cylinders  $z_n$  also needs to account for the change in the contact point according to Eq. (22).

$$L_n = L_0 - 2r_p \sin(\alpha) \quad (20)$$

$$a_n = a_0 - r_p \sin(\alpha) - r_p \sin(\beta) \quad (21)$$

$$z_n = z_a + r_p (1 - \cos(\alpha)) + r_p (1 - \cos(\beta)) \quad (22)$$

It is worth noting that with the new set of equations, a three-point bending test configuration can be considered as a particular case of a four-point bending test where the two upper cylinders share the same position, this is done by setting the initial geometric parameter  $a_0$  equal to  $L_0/2$ .

The procedure to compute the load-displacement curve for a three- or four-point bending test is explained as follows. The vertical displacement is gradually increased; this is done indirectly by imposing increasing values of  $\alpha$ . Then, for every value of  $\alpha$ ,  $L_n$  is updated according to Eq. (20), and the first estimation of  $\beta$  can be found by solving numerically Eq. (21) (using  $L_n$ , and approximating the first

value of  $a_n$  as  $a_0$ ). With an initial estimate of  $\beta$ ,  $a_n$  can be recalculated using again Eq. (21), this is an iterative process that is repeated until convergence is achieved in the values of  $\beta$  and  $a_n$ . Subsequently, the value of the relation  $2R/EI$  can be obtained from Eq. (12), this value is plugged in Eq. (15), setting  $\theta$  to zero to find the curvature at the middle of the beam span.

If the specimen is made of a composite laminate, where the  $x$  coordinate in Fig. 2 corresponds to the laminate  $x$  direction and the  $z$  coordinate in Fig. 2 to the thickness direction, the curvature  $1/r$  in Eq. (16) corresponds to the term  $\kappa_x$  in Eq. (8). If the values of  $N_x$ ,  $N_y$ ,  $N_{xy}$ ,  $M_y$ , and  $M_{xy}$  are set to zero (the layup is free to stretch as well as bend/twist when the deformation  $\kappa_x$  is imposed, this is consistent with the boundary conditions of a three or four-point bending test), the value of  $M_x$  can be found from Eq. (8), which, as explained previously, is equivalent to  $M$  in Eq. (16). So, having  $1/r$  and  $M$ , the product  $EI$  can be found in Eq. (16). The value of  $EI$  can be used to find the reaction load  $R$  of the lateral supports using Eq. (15). Then,  $z_a$  can be found from Eq. (13), and  $z_n$  from Eq. (22). Besides, having the reaction load in the lateral supports allows computing the reaction force  $F$  in the upper cylinders using Eq. (19). Note that at the beginning of the test, the angles  $\gamma$  and  $\lambda$  are 0. When the specimen deforms, the contact points move, and their location can be described with  $\gamma$  and  $\lambda$ . This algorithm was used to obtain the load-displacement and strain-displacement curves in the next sections. The algorithm has been implemented in a Python code and it is available upon request.

### 3. Methodology — validation and verification of the analytical model

The validation and verification of the analytical model were performed using experimental data results from previously published work [25,26] and two FE models (3D shell elements and 2D plane-strain elements) to demonstrate its reliability, robustness, and efficiency. In this section, the geometric setup, mechanical properties data, layup distribution and test configurations for validation are shown. Then, the numerical model parameters, boundary conditions and assumptions used for verification are explained in detail. Finally, the analytical, numerical, and experimental results are compared to demonstrate the accuracy of the new analytical approach. Once both analytical and FE models are validated, they are used in Section 4 to conduct “virtual tests”, i.e., FE models for different material configurations, to explore in more detail the implications of non-linearities in the interpretation of results according to the ASTM standards.

#### 3.1. Experimental bending test data

The first set of experimental data was chosen to validate the analytical model in the four-point configuration, accounting for large deformations, non-linear response, and a combination of different materials. On the other hand, with the second set of experimental data, it was possible to validate the three-point bending configuration and the use of different ply orientations.

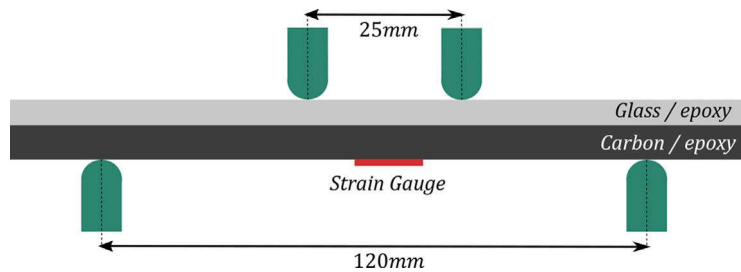


**Fig. 3.** Schematic of the four-point bending (4-PB) test setup [25].

**Table 1**  
Material properties [25–27].

Material	$E_1$ (GPa)	$E_2$ (GPa)	$\nu_{12}$ (–)	$G_{12}$ (GPa)	Thickness (mm)	$\epsilon_{tens}$ (%)	$\epsilon_{comp}$ (%)
SGlass-913/Epoxy	45.6	15.4	0.30	4.3	0.1551	3.98	2.33
T1000/Epoxy	143.3	6.06	0.32	2.4	0.3230	2.2	1.1
M55/Epoxy	280.0	6.06	0.32	2.4	0.0305	0.8	0.46 – 0.56
IM7/Epoxy	152.0	6.06	0.32	2.4	0.1300	1.6	1.23
Carbon/Epoxy (Exp. 2)	125.0	8.50	0.30	3.4	0.1980	–	–

### 3.1.1. Experimental data 1

The first set of experimental results comes from four-point bending tests on a hybrid composite laminate, in which non-linear behavior of the specimen and large elastic deformations prior to failure are evidenced [25]. The ply materials used in the experiment were high-performance unidirectional thin plies of carbon and glass fibers oriented at 0°; the layup configuration was [SGlass<sub>7</sub>/ T1000/ M55/ T1000<sub>2</sub>/ (T1000<sub>2</sub>/ M55/ T1000<sub>2</sub>)<sub>10</sub>], this type of distribution was used to obtain gradual failure on bending tests [25]. The test setup is shown in Fig. 3, and the mechanical properties of the materials are summarized in Table 1. From these tests, it was possible to obtain measurements of the vertical displacement of the upper cylinders, reaction loads from the load cell, and tensile strain on the lowest bottom carbon ply where one strain gauge was attached as shown in Fig. 3.

### 3.1.2. Experimental data 2

A three-point bending test of a unidirectional carbon-epoxy composite material was chosen for the second set of experimental data. The stacking sequence of the specimen was [45°/90°/−45°/0°]<sub>2S</sub> and the lateral support span in the test was 90 mm [26]. The mechanical properties of the material are also summarized in Table 1. In [26], the authors evaluate a scarf patch-repaired of the composite laminates, for this reason, only the load–displacement curve in the elastic regime was used for the validation of the analytical model. There was no direct strain measurement data available in this experimental campaign, thus the validation is performed using only the global stiffness of the specimen extracted from cross-head displacement and load cell data.

### 3.2. Finite element models setup

Two different types of FE analysis were used in order to obtain a broad perspective on the load–displacement, stress–strain behavior and evolution of the contact condition in the three- and four-point bending tests. Both FE methodologies account for large deformations and contact interaction with the upper cylinders and lateral supports, which are detailed later. The model imposed a displacement in the upper cylinders and then the reaction loads were extracted from the reference node where such displacement was imposed. In addition, strains on the bottom ply were obtained as average results on the nodes of the lowest bottom layer. The contact area and an equivalent contact point were also estimated based on the distribution of the contact pressure. It is worth mentioning that the numerical models, as well

as the analytical approach, can capture negative slopes in the load–displacement curve; this loss of structural stiffness is the result of large deformations of the specimen, and it is not related to material softening or damage, all the analyses consider only elastic material models. Setup and parametrization of these methodologies were done using a Python script to run a FE analysis in Abaqus CAE.

The 3D shell model allows the best numerical stability and convergence rate to simulate contact conditions in large deformations. The use of shell elements that do not consider out-of-plane stresses in the thickness direction, preserves the assumptions given in the CLT, allowing a reduced number of elements in the mesh as compared to 3D solid bricks and even 2D analysis, where the mesh size is restricted by the ply thickness. In this work, the specimen was modeled by a single layer of shell elements with quadratic formulation and full integration (SR8 in Abaqus), the same element type used in [6]. A mesh sensitivity analysis was performed and it was found that, for the specimen explained in the first set of experimental data of Section 3.1.1, the maximum element size required to obtain smooth and accurate load–displacement and strain–displacement curves is 1 mm, which corresponds to 1/10 of the diameter of the upper cylinders; larger mesh sizes can generate noise in the curves. The base geometry of the specimen needs to be a rectangular surface with no geometrical thickness imposed, because the thickness, as well as the stiffness, are given by the assignment of the layup section, see Fig. 4 A.

On the other hand, the 2D FE approach is not limited by the traditional assumptions of the shell element theories, this model allows more reliable approximations of stress and strain distributions along the thickness of the specimen. Thus, the 2D model can verify the thin plate assumptions made in the 3D shell model and the analytical approach. The 2D plane-strain elastic model considers a plane section for each lamina in the layup, the elements were quadrilateral eight-nodes for the specimen (CPE8 in Abaqus), and rigid lines were used to model the upper cylinders and lateral supports (Fig. 4 B). In this case, the mesh size is mainly limited by the thickness of the plies. According to the mesh sensitivity analysis, for the specimen explained in the first set of experimental data of Section 3.1.1, the maximum element size to obtain smooth and accurate load–displacement and strain–displacement curves is 0.03 mm, which corresponds to the thickness of the M55 ply; larger mesh sizes can generate noise in the curves. If the mesh size is close to the diameter of the upper cylinders, even the initial stiffness can be underestimated.

Both 2D and 3D shell FE models in Abaqus were set to account for geometric non-linearities (*NLgeom=on* in Abaqus) only. Thus, the

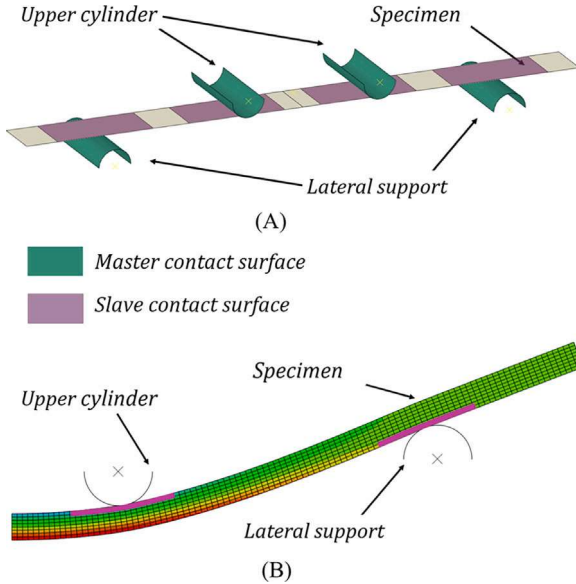


Fig. 4. FEA in Abaqus CAE (A) 3D shell and (B) 2D plane strain models.

material was always considered elastic no matter how high the strain values were. Also, for a specimen made out of a composite laminate, the material model needs to be anisotropic.

In order to account for geometric non-linearities Abaqus requires a hyper-elastic material model, which is by definition non-linear. In this case, it uses the St. Venant hyper-elastic material model, which is a direct extension from the standard Hooke's linear elastic model but that can give accurate results under large displacement and rotation as long as strains remain low [28]. In the St. Venant material model, the linear relation between the infinitesimal strain tensor and Cauchy stress tensor (from Hooke's linear elastic model) is replaced by the linear relation between the Green strain tensor and the Kirchhoff stress tensor. Thus, the stress and strain tensors in St. Venant and Hooke's law are related through the same linear elastic material tangent matrix which implies the same set of material properties extracted from mechanical testing considering infinitesimal elasticity assumptions. However, it should be bear in mind that even though the St. Venant material model recovers Hooke's linear elastic stress-strain relation in the limit of infinitesimal strains, St. Venant is a hyper-elastic material model and thus it is still non-linear because the Green-Lagrange strain tensor is a non-linear function of the displacement vector and the Cauchy stress tensor is a non-linear function of the Green-Lagrange strain tensor [28].

The St. Venant material model can be accurate if used with caution, thus the restriction of small strains should be respected. In this work, the limit of usability of the St. Venant model is set to 5% strain. The reason is that at 5% strain, the infinitesimal strain measure stops being accurate because the difference with finite strain metrics (more accurate strain metrics) becomes substantial [29]. Then, this is the point defined as the limiting value to consider infinitesimal strains as meaningful. Therefore, it is the limit strain value when the St. Venant material model and Hooke's laws become clearly dissimilar even in deformations that imply pure stretching. The good news is that the restrictions imposed by the St. Venant material model are exactly the same as those required by the assumptions made in the analytical model of Paolinelis and Ogorkiewicz [20], where the non-linear geometric effects are dealt with using solely geometrical analysis, while the material stiffness is considered assuming infinitesimal strains [20]. Within this context, the validation using the results of Idarraga et al. [25] becomes paramount as they provide the data from the strain gauges that validate the models by directly comparing strain measurements. This can be considered an additional guarantee of the accuracy of the models and

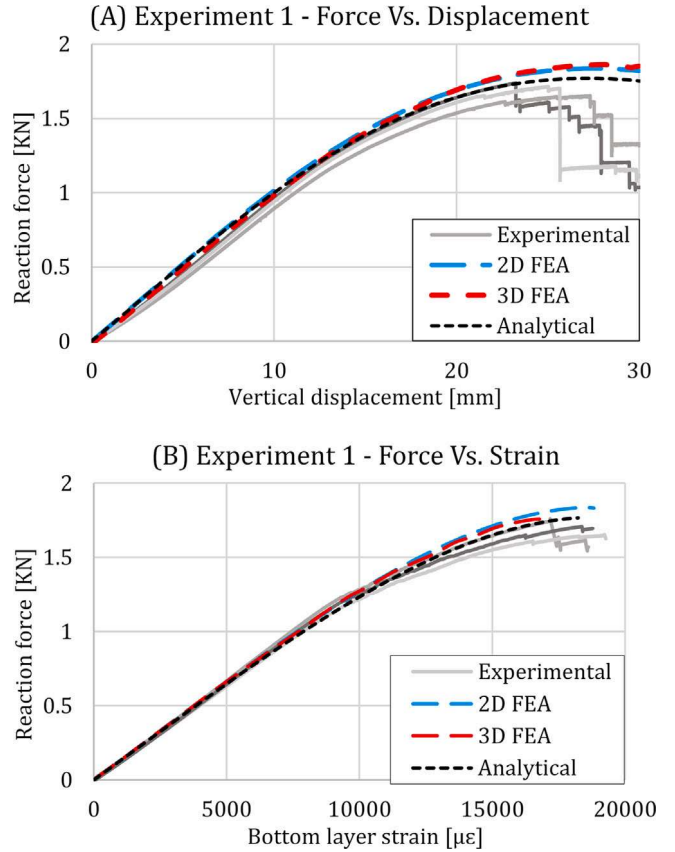


Fig. 5. (A) Force-Displacement and (B) Force-Strain curves, experimental [25], analytic, and FEA models for the hybrid composite material under four-point bending test.

assumptions, as the validation is performed using global information extracted from the loading machine and local information from the strain in the specimen. Therefore, it is ensured that the material model is properly selected and the assumptions made are valid.

Finally, for the numerical model it is necessary to say that the contact interaction uses a surface-to-surface discretization method and a finite sliding formulation. The contact interaction property was defined using a "Hard" contact condition for normal contact, where the constraint enforcement was done using a linear penalty method; while the tangential behavior was assumed as frictionless. The upper cylinders and lateral supports are the rigid surfaces that come into contact with the laminate, as required by Abaqus, the rigid surfaces are defined as master surfaces, while the slave surfaces are the areas of the layup that are most likely to come into contact, see Fig. 4.

### 3.3. Validation of analytical model and FE models

- For experiment 1:

The first part of the validation was done using a hybrid unidirectional and unsymmetrical layup in a four-point bending test under large displacements [25]. As it has become a common practice in numerical analysis, Fig. 5.A shows the load-displacement curves to validate by comparing the global stiffness prediction; this type of validation is purely performed from external data, which means cross-head reaction load and cross-head displacement is information taken exclusively from the testing machine and not directly from the specimen. At this point, one can only say that the overall stiffness of the specimen is correctly approximated from the beginning of loading until the specimen failure. Up to 12 mm of vertical displacement, the behavior is dominantly linear

with an overlap in the numerical and analytical predictions, showing that the initial stiffness is accurately predicted but with a small shift caused by contact initiation and settlement of the upper cylinders and the rubber that was used to diminish the likelihood of damage by contact. From 12 to 18 mm of vertical displacement, the non-linear response becomes evident, numerical and analytical predictions overlap, experimental results match the expected non-linear initiation and trend. From 18 mm of vertical displacement, the numerical predictions slightly deviate as the global stiffness is overpredicted by less than 5%; while the accurate match of the analytical prediction and experimental results is held up to failure initiation.

In addition to the validation using external data, Fig. 5.B also shows the evolution of the local measure of strain on the bottom ply measured with strain gauges in the experimental campaign, computed as the average value from the bottom nodes in the numerical model and approximated with CTL in the analytical model. In this case, it can be seen that both numerical and analytical models can accurately capture local information up to the failure of the specimens. Up to 8000 micro-strains, the behavior is dominantly linear; numerical and analytical predictions overlap with the experimental results. From 8000 to 12000 micro-strains, there is a shift to non-linear behavior that can be accurately captured with both approaches. From 13000 micro-strains on, numerical results deviate due to a slight overprediction of the reaction force (< 1%); while the analytical model overlaps the experimental results up to failure.

As explained previously, the usability of the St. Venant material model is restricted to strains below 5%, therefore it becomes essential to verify that the strains in all critical points remains below this threshold. As shown in Fig. 5 B, the strains in the central lower region where the strain gauge is located reach a maximum of 2% strain in tension which is in the safe region. Besides, the strains in the central upper region reach a maximum of 3.65% in compression. The maximum strains in the contact regions were monitored in all the simulations that were performed in this work, it can be ensured that the strains never went beyond the specified threshold of accuracy.

These results prove that numerical and analytical approaches can accurately capture the initial linear behavior and the initiation and evolution of non-linear responses extracted from the loading machine and the specimen strain. The strain gauge local measurements data validate the use of small strain and large deformation assumptions, supporting the assumptions made in the analytical model and in the selection of the St. Venant–Kirchhoff material model used in the FE analysis.

Since the numerical models do not consider damage, it is shown that most of the non-linear response (up to the first load drop) of hybrid composites could be caused by large deformations; the softening of the material due to the initial damage could provide just a very small contribution in the non-linear behavior in the test, see Fig. 5. This significant result helps to understand the mechanical behavior of pseudo ductile FRP composites.

The final verifications that need to be conducted to ensure all the assumptions made in the development of the analytical model can be considered accurate when four-point bending tests are studied using this new formulation are two: (i) the estimation of the contact angle and (ii) the accuracy of the small contact area assumption. For this, the contact angle and contact area have been estimated using the 2D FE model and compared with the analytic predictions. In the analytical model, the contact point is estimated according to Eqs. (20), (21) and (22), while in the FE analysis, the contact angle is defined as the point where the contact pressure is maximum (this parameter is defined in order to have a meaningful comparison with the analytical model) and the contact area is computed as the region where the contact pressure is larger than 5% the maximum contact pressure at a specific time step, see Fig. 6. The angle of maximum pressure is the value that should correspond to the contact angle in the analytical model. The comparison of the analytical contact angle and the numerically

estimated contact angle and contact area are plotted in Fig. 6 for the upper cylinders and lateral supports. This graph clearly shows that given the current definition of the contact point, the analytical model can accurately predict such a region even at large deformations; besides, the accuracy is well represented in both points of contact.

The variation of the contact length (contact in 2D FE analysis is limited to one line) can be estimated from the contact angles in Fig. 6. The length of these zones starts from zero. Then, it gradually increases, after 5 mm of vertical displacement the surface interaction reaches equilibrium and the contact length remains approximately constant for increased deformation. The longitude of this zone is larger in the upper cylinders as the contact pressure is higher on this area, nevertheless, the contact length does not go over 0.8 mm which represents only 2.5% of the perimeter of a circle with 5 mm radius. This is why it can be considered valid to use the assumption of contact in a single point in the new analytical formulation.

In order to have a more clear perspective on the augmented capabilities given by the new formulation; Fig. 7 shows a comparison of the original formulation proposed by Paolinelis and Ogorkiewicz in [20] (homogeneous material and fixed contact point) and the new formulation of the analytical model. The red line shows the prediction of the original model, for this curve, it was necessary to homogenize the properties of the hybrid laminate using the average of the longitudinal Young's modulus ( $E_1$ ) and Poisson's ratio ( $\nu_{12}$ ); the mean values were computed using the thickness of each layer as a weighting parameter (Position A11 of the ABB matrix of the CLT). The prediction of the original model is far from the one of the new formulation and from the experimental results. The main reason is that, in an unbalanced laminated where the SGlass layers (lower stiffness) are placed only on one side of the layup and they are stacked in an external position, the bending stiffness is much smaller than the longitudinal one, which is the stiffness used in the original isotropic model. However, this difference is much smaller in balanced laminates, for those scenarios, the initial part of the load–displacement curves is similar for the original and the new analytical models. Additionally, the result of including the Classical Laminate Theory (CLT) in Paolinelis and Ogorkiewicz original model, which is equivalent to the new analytical model used without assuming the contact interactions, was plotted with a blue line in Fig. 7. At the beginning of the loading process, when the deformation is small, the change in the contact points is very small, thus its influence on global stiffness is negligible. However, this effect becomes significant near the peak of the curve, where the original model over-predicts the compliance of the beam. Finally, the results of using the original model of Paolinelis and Ogorkiewicz including the contact interaction were plotted with a gray color. This curve is further away from the prediction of the new analytical model due to inaccurate material homogenization, as explained previously. Besides, in this case, the contact interaction increases the apparent stiffness of the beam, deviating even further from the experimental results.

- *For experiment 2:*

In addition to the validation using the data from hybrid unidirectional and unsymmetrical laminates, further validation was needed to confirm the predictive capabilities using more complex orientation distributions. Furthermore, the hypothesis of the possibility of using the same tools to model three-point bending tests needs to be verified. For these reasons, the results from the work of Truong et al. [26] on a quasi-isotropic layup in a three-point bending test were also considered to perform a rigorous validation of all the assumptions made.

The comparison of load–displacement curves obtained from the test machine in the experiment, FE analysis using 3D shell elements, and the analytical model are shown in Fig. 8. It can be seen that the behavior is mainly linear up to 3 mm of vertical displacement. In this region, the experimental results and numerical and analytical predictions overlap. However, from 3 mm on, the experiments show a slight non-linear

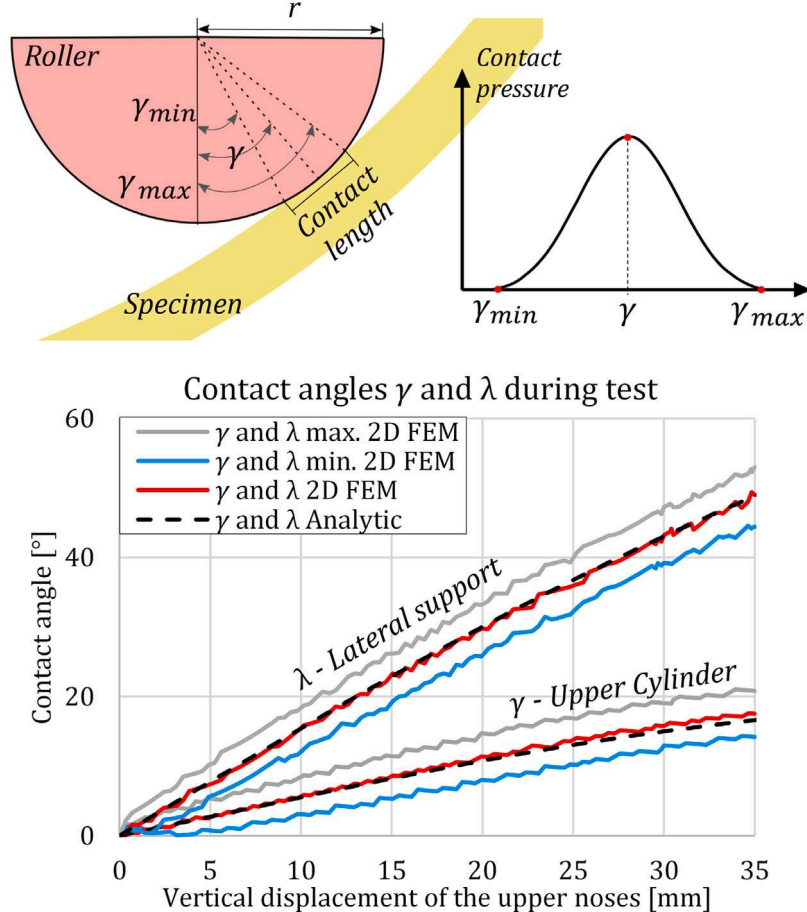


Fig. 6. Numerical and analytical predictions of the contact point and numerical estimation for the contact angle on the upper cylinders and lateral supports.

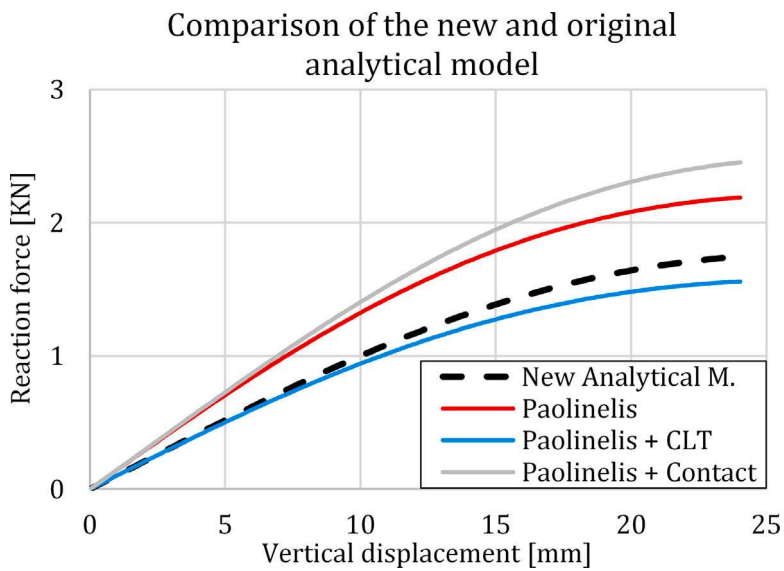


Fig. 7. Comparison between the predictions of the analytical model and the original one proposed in [20].

behavior as the curve tends to curve with a negative concavity. Such a trend is perceived in the analytical model but is not fully evident in the numerical model for such low vertical displacement. This proves that, even though the analytical approach is more sensitive to geometric non-linearities than the 3D shell model approach, both of them can estimate the stiffness in multidirectional laminates in a three-point bending test. In this case, the 2D plane strain model was not used, as the

multidirectional laminate does not allow plane-elasticity assumptions. Besides, strain measurements could not be compared as there were no available data.

Although the numerical models could accurately predict the behavior of both three- and four-point bending tests as previously demonstrated, the analytical model was more efficient because it did not require high computational resources and took about 1000 times less

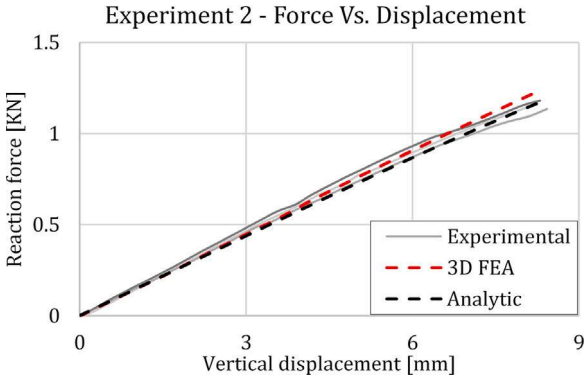


Fig. 8. Force–Displacement curve, experimental [26], analytical and FEA models for composite carbon material submitted to three-point bending test.

computation time than the 2D and 3D FE models. Moreover, as 2D FE simulations produce similar results to 3D ones, 2D can efficiently simulate “virtual tests” based on materials shown in Table 1. This will allow a detailed discussion of the interpretation of three- and four-point bending tests.

#### 4. Virtual bending test analysis

This section shows several predicted load–displacement curves, comparing different materials under different span-to-thickness ratios (STRs) to analyze the consequences of the test setup and material stiffness on geometric non-linearities due to large deformation. These curves were calculated by different modeling methods (3D shell, 2D plane, proposed analytical model) using the mechanical properties shown in Table 1. Moreover, the procedures and derivations suggested by the standards ASTM D6272-17 [4] and ASTM D7264M-21 [5] to calculate the strength of polymer-reinforced composite material during flexural tests are discussed, which may be incorrect when using low stiffness materials and large STR.

##### 4.1. Effect of material stiffness into non-linear behavior

Virtual tests using FE analysis and the proposed analytical method were performed using materials with different elastic modulus and STR setup configurations to discuss their relationship with the geometric non-linearities. These virtual tests were stopped at 1.5 times the maximum strain of the material to appreciate the presence of non-linearities better. The materials chosen for this purpose were the SGlass (low  $E$ ), IM7 (medium  $E$ ), and M55 (high  $E$ ); their mechanical properties are summarized in Table 1. On the other hand, the virtual tests were made using three STR setup configurations recommended by the standards, 32:1, 40:1, and 60:1. All the tests were performed on specimens with an equal thickness (4 mm) and width (13 mm) according to the recommendations in the standard. Hence, in practice, only the initial support span  $L_0$  changes when choosing a different STR.

Figs. 9 and 10 shows the load–displacement and load strain curves, respectively, of a three-point bending case for the three different materials using the three different STR. It is evident that materials with lower stiffness and test geometries with greater spans tend to present non-linearities due to large deformations. Although the SGlass is a linear elastic material, the results showed geometrical non-linearities even for the lowest STR (32:1) due to its low stiffness. It is worth mentioning that the elastic modulus of SGlass is similar and in some cases higher to materials such as resins, thermoplastics, or natural fiber composites; therefore, these materials would obtain similar non-linear behavior in this test setup. In contrast, stiffer materials like the IM7 only showed non-linearities for the higher STR. Finally, the M55

laminate shows linear behavior in the three test setups as a consequence of being the stiffest material.

Incidentally, Fig. 9 also helps show the excellent general accordance between the three different modeling methods throughout all the test setups and materials, further verifying the capacities of the proposed analytical method. However, it becomes necessary to highlight the potential limitations of the plane strain elasticity assumptions as well as the hyper-elastic material model used in FE analysis. For instance, for the material with the lowest modulus and highest non-linear behavior, the numerical predictions overestimate the stiffness if compared to the analytical approach. Such deviation is more pronounced as the concavity of the curve increases, as in this case, higher strains are reached, and the range of functionality of the St. Venant–Kirchhoff material model is close to being trespassed. This effect is stronger for lower STRs and higher deformations, suggesting that higher strains are imposed. Besides, in the regions of higher concavity, the differences between the plane strain and 3D shell models become evident, as the Poisson’s effect after large deformations increases the stiffness even more due to the plane-strain assumption.

On the other hand, the trend for the material with the highest Young’s modulus is the opposite; the numerical models underpredict the stiffness while no deviation between 2D and 3D approaches is observed. In this case, lower STRs combined with larger vertical displacements also imply higher deviations between numerical and analytical methods, but the contact interaction with a harder material may need adjustments with a higher penalty to reach the same deformations as is the case in the analytical model. The best match is observed on materials with medium modulus such as IM7/Epoxy, as in this case, the stress–strain behavior remains in the range of functionality of St. Venant–Kirchhoff material model and the stiffness of the material produces a contact interaction close to the behavior assumed in the analytical model. Further investigations are needed to properly delimit the range of functionality of the numerical and analytical approaches.

##### 4.2. ASTM implications for flexural properties calculations

Among the currently valid standards for performing the testing of flexural properties of polymer matrix components are those of ASTM [4, 5], which specify all the adequate parameters and conditions for performing such tests, as well as providing tools for determining the flexural properties (strength, stiffness, load/deflection behavior) of polymer matrix composite materials. The default value of the span-to-thickness ratio (STR) is suggested as 32:1, but optional STRs of 16:1, 20:1, 40:1, and 60:1 are allowed to provide a wider range of testable specimens. As shown in the previous section, tests with higher STRs are more susceptible to the presence of geometric non-linearities due to large deformations.

The standards state that the maximum stress and strain state at the outer surface occurs at mid-span; we will refer to these quantities as Standard Stresses ( $\sigma_{ASTM}$ ) and Standard Strains ( $\epsilon_{ASTM}$ ), calculated with Eqs. (23) and (24), respectively. A clear distinction ought to be made between these quantities and the ones defined as Local Stress ( $\sigma_{loc}$ ) and Local Strain ( $\epsilon_{loc}$ ), which refer to the “real” values of stress and strain, that is, the ones obtained by the analytical and numerical models, for instance.

$$\sigma_{ASTM} = \frac{3F_z L}{C_1 b h^2} \quad (23)$$

$$\epsilon_{ASTM} = \frac{C_2 Z_n \delta h}{L_2} \quad (24)$$

In Eqs. (23) and (24),  $F_z$  corresponds to the load magnitude measured by the load cell in  $N$ ,  $L_0$  to the initial support span in mm,  $b$  to the width of the beam in mm,  $h$  to the thickness of the specimen in mm,  $Z_n \delta$  to the vertical displacement measured in the cylinders to the maximum deflection assumed as the cross-head displacement in mm; and  $C_1$  and  $C_2$  constants that correspond to 2 and 6, respectively, for

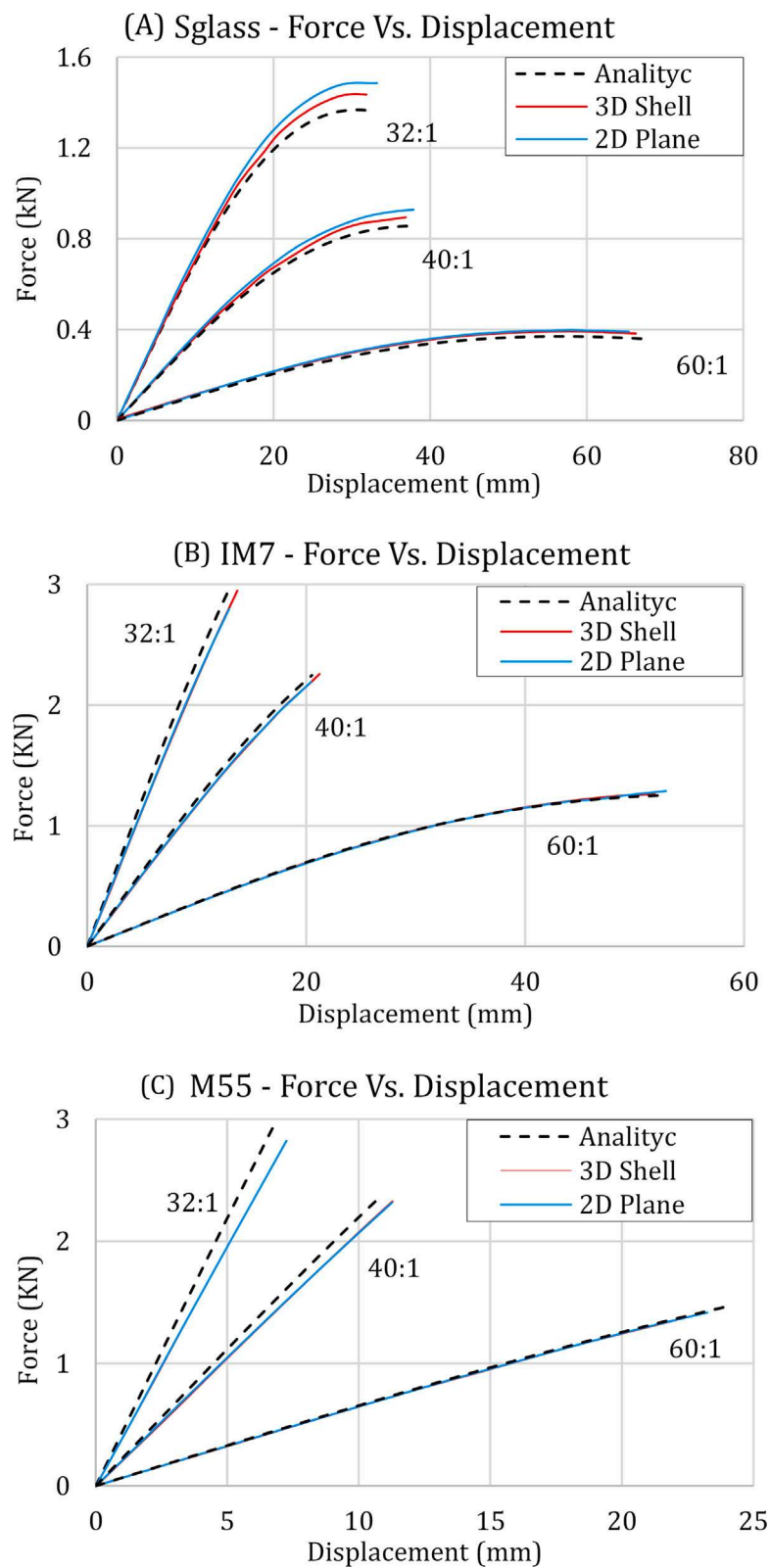


Fig. 9. Virtual tests for the three materials and three STR — Force Vs. Displacement curves: (A) SGlass/Epoxy, (B) IM7/Epoxy and (C) M55/Epoxy.

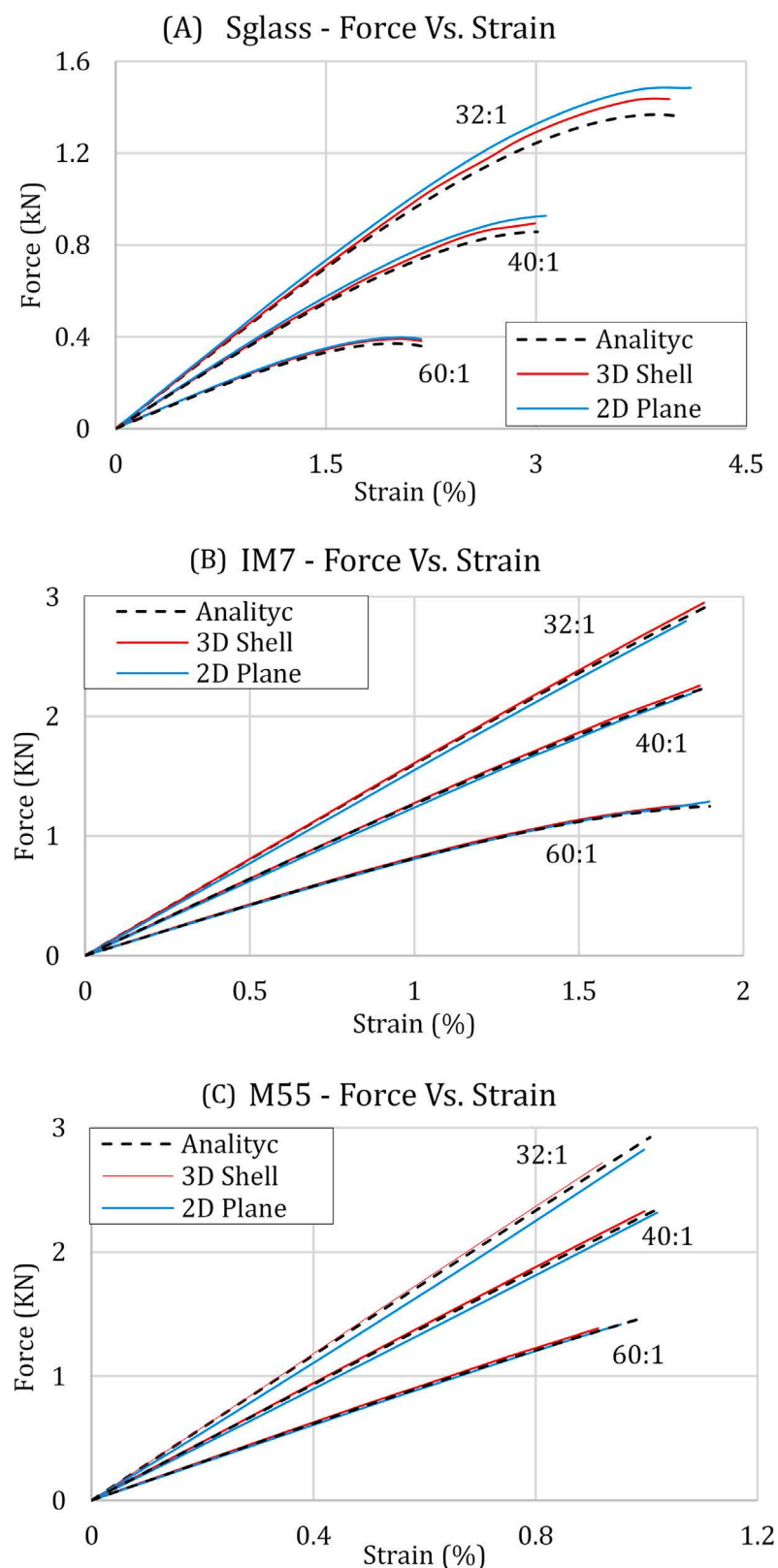


Fig. 10. Virtual tests for the three materials and three STR — Force Vs. Strain curves: (A) SGlass/Epoxy, (B) IM7/Epoxy and (C) M55/Epoxy.

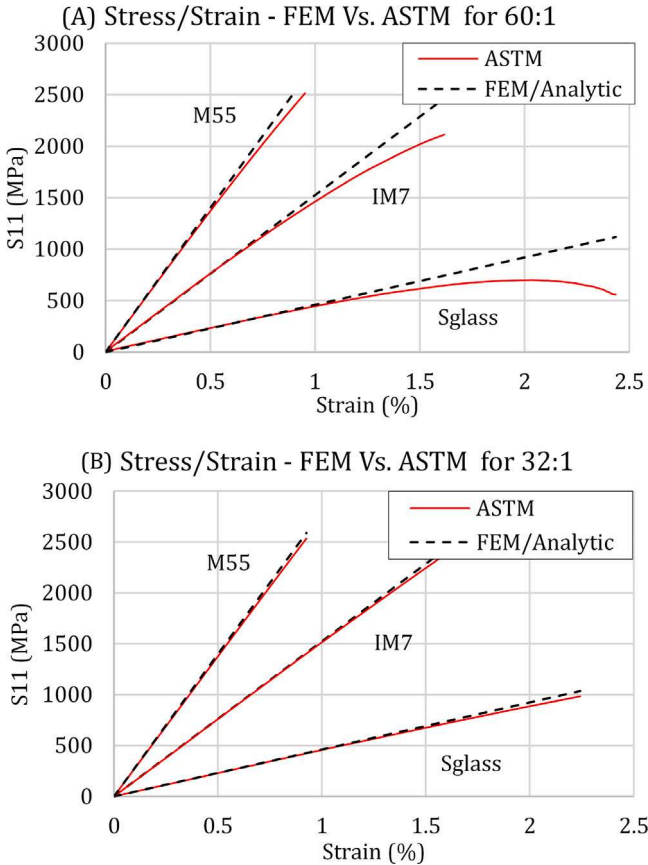


Fig. 11. Comparison between Local and Standard stress-strain curves of materials with a STR of (A) 60:1 and (B) 32:1.

the three-point-bending case; and to 4 and 4.36, respectively, for the four-point-bending case. As shown below, the geometric non-linearities induced by large deformations can obscure accurate measurements of mechanical properties, and Eqs. (23) and (24) must be used with caution.

Fig. 11 compares the  $\sigma_{ASTM} - \varepsilon_{ASTM}$  curves with the corresponding  $\sigma_{loc} - \varepsilon_{loc}$  curves. The geometric non-linearities strongly affect the accuracy of the Stress–Strain behavior predicted using the standard. It is shown that as non-linearities increase, the stress prediction highly deviates from realistic stress value. This phenomenon has little or no effect on stiffer materials and smaller support spans, as shown in Fig. 11 for an STR of 32:1. However, this figure shows that even the stiffest materials suffer this effect when a larger STR (60:1) is used.

These results demonstrate that the methods suggested by the standard to calculate the flexural maximum strength and strain of composite material should be analyzed with care when using high STR and low stiffness materials. The miscalculation of these mechanical properties can lead to poor design and material selection decisions.

Given the fact that the linear behavior of the material is used in the analytical and numerical analyses, the only non-linearities allowed are those of geometric origin due to large deformations and contact interactions. These can be observed in the force–displacement curves. However, it is important to note that, although results in Fig. 5 suggest that most of the non-linear effect comes from geometrical aspects, damage can still contribute to the observed non-linear behavior in real experiments, though for the hybrid-composite samples used to validate the present analytical model, this contribution seems to be negligible up to the first visible load drop. Further experiments considering other damage-capturing measurements, like acoustic emission or in-situ X-ray tomography bending test, are necessary to fully understand the damage effect on non-linearities in hybrid composite materials.

## 5. Conclusions

An analytical model for predicting the elastic behavior of composite beams when submitted to three- and four-point bending loading that present non-linearities due to large deformations was introduced. The model extends the capabilities of a previous one presented by Paolinelis and Ogorkiewicz in [20], limited to isotropic materials, to composite materials ranging from stiff to compliant ones. The analytical model was validated using the force, displacement, and strain experimental results reported by different authors; and verified using two Finite Element approaches in Abaqus CAE, the 2D plane-strain and the 3D shell numerical models.

The proposed analytical model takes the material properties, stacking sequence, specimen, and test setup geometry as the input variables and numerically obtains a relation between the applied load and mid-span deflection using the Classical Laminate Theory (CLT) and non-linear beam theory. The model presents a great advantage when investigating the non-linearities in bending of linear elastic composite material beams compared with the FE models due to ease of use and solution time. It avoids the necessity to set up FE simulations which are time-consuming, and on top of that, calculates accurate results in a matter of seconds, as opposed to several hours on some very refined 2D FE models in which the inclusion of geometric non-linearities significantly increases solution time.

The effects of material stiffness and test setup geometry on the prevalence of geometric non-linearities due to large deformations were investigated using the proposed model. Materials with low stiffness and specimens with large STR presented marked non-linear behavior and large deformations. It was demonstrated that ASTM standards equations for flexural stress calculation (Standard Stresses) of composite beam with low stiffnesses or larger STR can underestimate the specimens' real stress state (local stresses). This can lead to non-accurate design processes of components that might be critical to a structure. On the other hand, stiffer materials and shorter STR present a behavior close to a true linear behaviour, and ASTM standard equations can be used without concerns.

## CRediT authorship contribution statement

**Juan Macías:** Conceptualization of this study, Methodology, Implementation, Analysis, Writing – original draft, Writing – review & editing. **Santiago Marín:** Conceptualization of this study, Methodology, Implementation, Analysis, Writing – review & editing. **Juan Meza:** Conceptualization of this study, Methodology, Analysis, Writing – review & editing.

## Declaration of competing interest

The authors declare the following financial interests/personal relationships which may be considered as potential competing interests: Juan Macías reports financial support was provided by Royal Academy of Engineering.

## Data availability

Data will be made available on request.

## Acknowledgments

This work was funded under the UK Royal Academy of Engineering and Newton Fund under contract IAPP\1516\140. Special acknowledgments to Dr. Meisam Jalalvand and Dr. Guillermo Idarraga for their experimental results and their contributions to the development of this work. J. Meza acknowledges Universidad Nacional de Colombia, Colombia for the support through LTDM Laboratory.

## References

- [1] William G, Branko S, Max U. Composite structures: the first 100 years. Int conf composites mater 2007;16th.
- [2] Swolfs Yentl, Verpoest Ignas, Gorbatikh Larissa. Recent advances in fibre-hybrid composites: materials selection, opportunities and applications. Int Mater Rev 2019;64(4):181–215.
- [3] Recupero Antonio, D'Aveni Antonino, Ghersi Aurelio. Bending moment-shear force interaction domains for prestressed concrete beams. J Struct Eng 2005;131(9):1413–21.
- [4] ASTM International. ASTM D6272-17e1, standard test method for flexural properties of unreinforced and reinforced plastics and electrical insulating materials by four-point bending. West Conshohocken; 2017.
- [5] ASTM International. ASTM D7264 / D7264M-21, standard test method for flexural properties of polymer matrix composite materials. 2021, West Conshohocken.
- [6] Kalantari Mehdi, Dong Chensong, Davies Ian J. Numerical investigation of the hybridisation mechanism in fibre reinforced hybrid composites subjected to flexural load. Composites B 2016;102:100–11.
- [7] Dong Chensong. Uncertainties in flexural strength of carbon/glass fibre reinforced hybrid epoxy composites. Composites B 2016;98:176–81.
- [8] Dong Chensong, Davies Ian J. Optimal design for the flexural behaviour of glass and carbon fibre reinforced polymer hybrid composites. Mater Des 2012;37:450–7.
- [9] Dong Chensong, Davies Ian J. Flexural properties of glass and carbon fiber reinforced epoxy hybrid composites. Proc Inst Mech Eng L 2012;227(4):308–17.
- [10] Dong Chensong, Davies Ian J. Flexural and tensile strengths of unidirectional hybrid epoxy composites reinforced by S-2 glass and T700s carbon fibres. Mater Design (1980-2015) 2014;54:955–66.
- [11] Jalalvand Meisam, Czél Gergely, Wisnom Michael R. Numerical modelling of the damage modes in UD thin carbon/glass hybrid laminates. Compos Sci Technol 2014;94:39–47.
- [12] Reis PNB, Ferreira JAM, Antunes FV, Costa JDM. Flexural behaviour of hybrid laminated composites. Composites A 2007;38(6):1612–20.
- [13] Greco Fabrizio, Leonetti Lorenzo, Pranno Andrea, Rudykh Stephan. Mechanical behavior of bio-inspired nacre-like composites: A hybrid multiscale modeling approach. Compos Struct 2020;233:111625.
- [14] Laurin F, Carrère N, Maire J-F. A multiscale progressive failure approach for composite laminates based on thermodynamical viscoelastic and damage models. Composites A 2007;38(1):198–209.
- [15] Greco Fabrizio, Leonetti Lorenzo, Lonetti Paolo, Luciano Raimondo, Pranno Andrea. A multiscale analysis of instability-induced failure mechanisms in fiber-reinforced composite structures via alternative modeling approaches. Compos Struct 2020;251:112529.
- [16] Bruno Domenico, Greco Fabrizio, Luciano Raimondo, Nevone Blasi Paolo. Nonlinear homogenized properties of defected composite materials. Comput Struct 2014;134:102–11.
- [17] Benbouras Youssef, Bellahkim Mouad, Maziri Aziz, Mallil Elhassan, Echaabi Jamal. Nonlinear modeling of the failure of a graphite epoxy under a three-point bending test. Polym Polym Compos 2019;28(2):119–39.
- [18] Benbouras Youssef, Maziri Aziz, Mallil Elhassan, Echaabi Jamal. A nonlinear analytical model for symmetric laminated beams in three-point bending. Int J Technol 2017;8(3).
- [19] Badriev IB, Makarov MV, Paimushin VN. Mathematical simulation of nonlinear problem of three-point composite sample bending test. Procedia Eng 2016;150:1056–62.
- [20] Paolinelis SI, Ogorkiewicz RM. Large deflections of beams in four-point bending. J Strain Anal Eng Des 1976;11(3):144–9.
- [21] Barbero Ever J. Introduction to composite materials design. 3rd ed.. Boca Raton: CRC Press; 2017, p. 570,
- [22] Barbero Ever J. Finite element analysis of composite materials using abaqus. 1st ed. CRC Press; 2013, p. 444,
- [23] Kalantari Mehdi, Dong Chensong, Davies Ian J. Multi-objective analysis for optimal and robust design of unidirectional glass/carbon fibre reinforced hybrid epoxy composites under flexural loading. Composites B 2016;84:130–9.
- [24] Megahed K. Introduction to nonlinear finite element analysis. Zenodo; 2019.
- [25] Idarraga Guillermo, Jalalvand Meisam, Fotouhi Mohamad, Meza Juan, Wisnom Michael R. Gradual failure in high-performance unidirectional thin-ply carbon/glass hybrid composites under bending. Compos Struct 2021;271:114128.
- [26] Truong Viet Hoai, Kwak Byeong Su, Roy Rene, Kweon Jin Hwe. Cohesive zone method for failure analysis of scarf patch-repaired composite laminates under bending load. Compos Struct 2019;222:110895.
- [27] Czél Gergely, Jalalvand Meisam, Wisnom Michael R. Design and characterisation of advanced pseudo-ductile unidirectional thin-ply carbon/epoxy-glass/epoxy hybrid composites. Compos Struct 2016;143:362–70.
- [28] Wriggers Peter. Nonlinear finite element methods. Springer Berlin Heidelberg; 2008, 1–559.
- [29] Kim Nam Ho. Introduction to nonlinear finite element analysis. Springer US; 2015, 1–430.